atmosphere

MDPI

Article

Assessing the Impact of Climate Change on Intensity-Duration-Frequency (IDF) Curves for the Qassim Region, Saudi Arabia

Mohammed ALRakathi and Abdullah Alodah *

Department of Civil Engineering, College of Engineering, Qassim University, Buraidah 51452, Qassim, Saudi Arabia
* Correspondence: aalodah@qu.edu.sa

Abstract: Climate change has the potential to significantly impact various aspects of Earth's climate systems, including precipitation patterns, necessitating region-specific action plans. This study examines the Wadi Al Rummah region in Qassim province, Saudi Arabia, by analyzing Intensity-Duration-Frequency (IDF) curves across six locations, utilizing observed daily precipitation data from 1986 to 2014. The nonparametric quantile mapping method was employed to adjust the outputs of eight Regional Climate Models (RCMs) within the CMIP6 ensemble. These models were evaluated under four Shared Socioeconomic Pathways (SSPs), ranging from a stringent mitigation scenario to one with very high greenhouse gas emissions. Also, two statistical tests, namely the Kolmogorov-Smirnov and Chi-Square tests, were used to assess the best-fitting distribution to estimate the maximum rainfall values. Temporal disaggregation of daily precipitation data was performed using the K-nearest neighbors (KNN) method. The IDF curves were generated for both historical and three projected future periods using Gumbel distribution, which proved to be the best-fitting statistical model, using six return periods: 2, 5, 10, 25, 50, and 100 years. Results indicate that high-emission scenarios and longer timeframes exhibit greater uncertainty in IDF projections. Additionally, rainfall intensity is expected to increase over shorter durations, with significant increases observed in Buriydah and Nabhaniyah under SSP 8.5. In contrast, Al Rass, Badayea, and Al Mithnab show mixed trends, while Unaizah shows little to no significant change. These findings emphasize the need for sustainable development and adaptive strategies to mitigate risks in Qassim province, as climate impacts are projected to intensify, particularly in the short to long term.

Keywords: intensity-duration-frequency curves; IDF; climate change; temporal disaggregation; quantile mapping; RCMs

check for updates

Academic Editors: Cristian Anghel and Xiong Zhou

Received: 1 December 2024
Revised: 21 December 2024
Accepted: 22 December 2024
Published: 8 January 2025

Citation: ALRakathi, M.; Alodah, A. Assessing the Impact of Climate Change on Intensity-Duration-Frequency (IDF) Curves for the Qassim Region, Saudi Arabia. *Atmosphere* **2025**, *16*, 59. https://doi.org/10.3390/atmos16010059

Copyright: © 2025 by the authors. Licensee MDPI, Basel, Switzerland. This article is an open access article distributed under the terms and conditions of the Creative Commons Attribution (CC BY) license (https://creativecommons.org/licenses/by/4.0/).

1. Introduction

The intensity-duration-frequency (IDF) curves are essential tools in hydrology and infrastructure design, helping engineers analyze rainfall patterns and their potential impacts on urban water systems. With the growing effects of climate change, precipitation patterns are likely to be altered, resulting in more intense and frequent rainfall events in many regions [1].

Climate change, predominantly driven by human activities such as fossil fuel combustion, leads to long-term alterations in average weather patterns. Since the mid-20th century, the Earth's climate has been warming, with global temperatures estimated to have increased by over 1.0 °C above pre-industrial levels [2]. These alterations are evident in rising global temperatures, sea levels, and atmospheric carbon dioxide concentrations, indicating a

persistent trend unless mitigative actions are implemented [3]. The evidence for observed changes, in particular, in the dynamics of extreme precipitation events—such as heavy precipitation and droughts—has strengthened, according to the Intergovernmental Panel on Climate Change (IPCC) Sixth Assessment Report (AR6) [4].

Locally, recent observations of heavy rain events in the Qassim region have raised serious concerns about the impacts of climate change. Despite its highly arid conditions, the area has seen an increase in the frequency and intensity of heavy rain events over the past decade, resulting in an unprecedented number of occurrences of flows in the ephemeral Wadi Al Rummah that drains the region. Warming trends across Saudi Arabia, particularly over the past four decades [5].

Climate projections, represented by Representative Concentration Pathways (RCPs) and more recently by the Shared Socioeconomic Pathways (SSPs), help explore potential future climate scenarios. These projections illustrate the impacts of varying greenhouse gas emissions, where high emissions scenarios predict a doubling of CO_2 emissions by 2100 [6]. The effects of climate change on precipitation patterns are increasingly apparent, with models suggesting intensified evaporation resulting in more frequent and intense storms in certain regions while simultaneously causing droughts in others [7]. In Saudi Arabia, future projections predict an annual temperature increase with diverse impacts on precipitation across the country [1]. Based on multi-model analysis in Saudi Arabia, mean annual precipitation is expected to rise significantly, up to 45% over the long term, particularly under high-emission scenarios SSP5-8.5 and SSP3-7.0 [8]. Nevertheless, the diverse outcomes across the country underscore the necessity for region-specific assessments [9–13].

Regional Climate Models (RCMs) play a crucial role in climate change modeling by providing high-resolution models driven by climate simulations of Global Climate Models (GCMs) that focus on specific regions. They can simulate local climate processes, such as topography, land-sea contrasts, and regional atmospheric circulation patterns, offering finer-scale projections of climate variables like temperature and precipitation. However, RCMs still suffer from biases and limited resolution. Downscaling techniques, whether dynamical (enhancing the resolution of GCM/RCM outputs) or statistical (relating model output to observed data), help refine these projections for more accurate regional and local climate impact assessments [14–16]. Statistical downscaling methods use empirical relationships between observed and climate model data to adjust biases and refine spatial resolution, with the assumption that these relationships remain stationary over time.

In the context of generating IDF curves, Goodness-of-Fit (GoF) is a crucial tool for validating the reliability and accuracy of the curves produced. Various studies have identified statistical distributions that best fit IDF curves across Saudi Arabia, with findings indicating that the Gumbel Type I distribution is particularly suitable for the Makkah Al Mukarramah region [17]. Similarly, the Gamma distribution has been recommended for the Jeddah region [18], while comparisons between the log-Pearson Type III and Gumbel distributions across various regions in western Saudi Arabia have yielded differing results, emphasizing the role of local climatic factors in selecting the most suitable models [19–21]. However, there is a significant gap in research on IDF curves for Qassim province and central Saudi Arabia, highlighting the need for studies that identify the most suitable statistical models for accurately representing rainfall patterns in this region.

The generation of IDF curves necessitates high-resolution temporal rainfall data; however, when historical records at such fine scales are unavailable, rainfall disaggregation presents a viable solution [22,23]. This approach applies theoretical probability distribution functions to variables such as the daily number of events, start times, volume, and duration [24–26]. Another group of techniques is based on rectangular pulse stochastic

rainfall models [27–29]. Additionally, disaggregation can be accomplished using artificial neural network models grounded in the theory of learning [30] or a chaotic model [31,32]. Rainfall statistics' scaling properties offer a helpful framework for disaggregation, facilitating shifts from existing data scales to those needed in hydrological applications. These approaches provide practical applications in urban hydrology, and help meet the need for more granular data, especially in hydrological models [33].

This study provides the first comprehensive analysis of Intensity-Duration-Frequency (IDF) curves in the Qassim region, addressing a critical research gap and significantly enhancing our understanding of how climate change affects precipitation patterns. Unlike many other regions worldwide [34], daily climate datasets in the Arabian Peninsula have not been widely utilized to analyze the variability of extreme weather events. The primary objective of this study is to generate IDF curves for both the historical period and four distinct future climate scenarios. These scenarios include a stringent mitigation scenario (SSP 2.6), two intermediate scenarios (SSP 4.5 and SSP 7.0), and one scenario characterized by very high greenhouse gas emissions (SSP 8.5). Specific goals include implementing bias correction for Regional Climate Model (RCM) outputs using nonparametric quantile mapping, examining changes in the frequency and intensity of precipitation, and conducting a comparative assessment of projections from eight different climate models to improve our understanding of precipitation variability.

2. Materials

2.1. Study Area

Wadi Alrummah is crucial in Saudi Arabia and is the most significant and prolonged wadi on the Arabian Peninsula. The wadi begins on the eastern slopes of the Al Abyad Mountains and from the nearby Harat foothills, located on the edges of the Medina Region. It flows northeast, merging with multiple tributaries from the north and south until it is blocked by the dunes of Nfood Al Thwairat in the Dahna desert, near the village of Bandariah, south of Asyah in the Qassim Region. Spanning about 600 km from its origin to its mouth, the wadi is a channel for gathering and directing runoff water through an intricate network of tributaries.

According to Sultan [35] and Al-Gurairy et al. [36], Wadi Alrummah can be divided, based on the physical geography and drainage system, into four integrated sections: (A) Upstream (Arab Shield), (B) Midstream, (C) Al-Nafud Desert, and (D) Downstream. It's worth noting that most of the Wadi basin is situated within the Qassim Region. Within the Qassim Region, the boundaries of Wadi Alrummah become more pronounced, exhibiting a meandering path with varying widths. In this research, the analysis is carried out mainly for section B, which is the Qassim region. Figure 1 shows sections A and B of the watershed of Wadi Alrummah, mostly in the Qassim region, as well as the location of meteorological stations used to collect the observed data.

Qassim Province, situated near the geographic center of the Arabian Peninsula, had a population of 1,336,179 in 2022 [37]. The area is distinguished by long, hot summers and mild winters. Summer temperatures can reach 45 °C, while winter temperatures usually range between 10 °C and 20 °C. The region receives relatively low annual rainfall, and the rainy season typically occurs between November and April, with most of the rainfall occurring in the winter months.

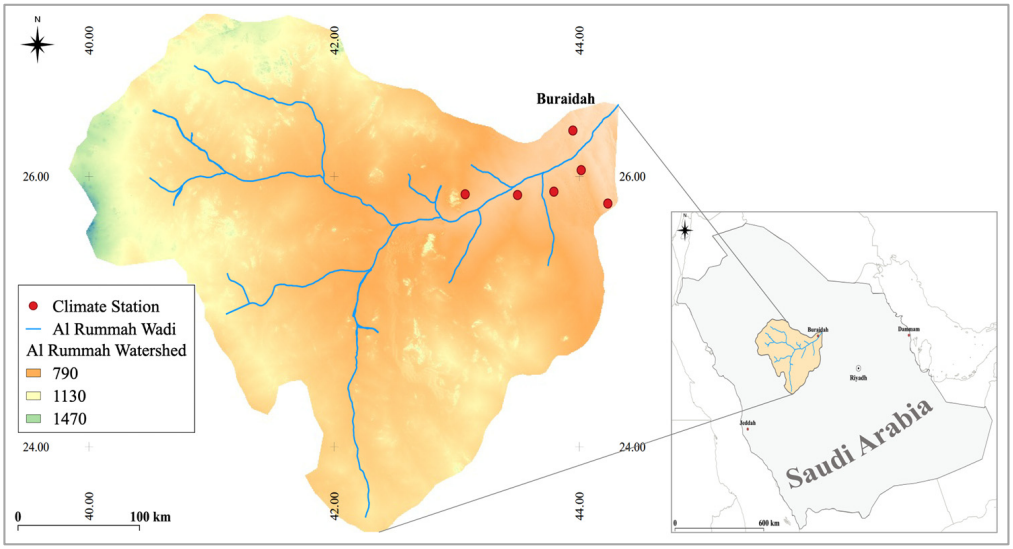


Figure 1. Location of the study area and the meteorological stations (colors indicate the elevation in meters above sea level).

2.2. Data Collection

2.2.1. Meteorological Stations

Meteorological stations play a vital role in collecting and preserving historical data, which is essential for predicting future meteorological conditions. However, this study area faces a significant challenge due to the limited availability of climate data, hindering effective environmental analysis and planning. This study utilized observed data from all available meteorological stations to allow for model adjustments and corrections. From 1986 to 2014, precipitation data (PCP) was collected from six stations, mainly located on the downstream. The summary of the used stations, as presented in Table 1, indicated that the average altitude was about 685 m above sea level, while the average PCP values of mean and maximum daily data were determined to be 0.26 mm and 78.63 mm, respectively. Moreover, the mean annual precipitation in the region typically averages around 60–130 mm, reflecting its arid climate and seasonal rainfall patterns.

Table 1. Summary of observed data for all stations.

Station	Longitude	Latitude	Altitude	Mean Daily PCP	Max Daily PCP	Mean Annual PCP
	East	North	m	mm	mm	mm
Buraidah	43.76753°	26.30778°	647.00	0.32	80.80	115.70
Al Rass	43.45180°	25.83143°	672.00	0.22	70.00	84.84
Al Nabhaniyah	43.04705°	25.87007°	753.00	0.18	73.20	61.98
Al Mithnab	44.22171°	25.83577°	636.00	0.24	80.80	84.58
Onaizah	43.99920°	26.06980°	678.00	0.33	83.80	127.66
Al Badayea	43.81450°	25.88190°	725.00	0.30	83.20	110.97
Average			**685.17**	**0.26**	**78.63**	**97.62**

2.2.2. Regional Climate Model Data

Regional climate models (RCMs) are a critical tool for understanding and addressing the complex dynamics of climate change. RCMs, with their high spatial resolution, offer more accurate, localized climate predictions than global climate models (GCMs), making them essential for analyzing regional climate variability, the effects of land use changes, and localized climate change impacts [38]. In essence, RCMs are instrumental in shaping regional climate policies, guiding adaptation strategies, and empowering us to make informed decisions to protect and enhance the well-being of our communities

and ecosystems. This research collected data from eight models from 1986 to 2100 in the CMIP6 dataset (data source: https://esgf-node.llnl.gov/projects/cmip6/, accessed on 30 August 2023). Table 2 demonstrates the regional climate models employed in the current study. The eight models that were chosen for analysis are BCC-CSM2, CESM2, EC-Earth3, FGOALS-g3, GFDL-ESM4, INM-CM5, MIROC-ES2L, and NorESM2-MM, each containing Shared Socioeconomic Pathways (SSPs) 2.6, 4.5, 7, and 8.5. In the study, four distinct periods were simulated: the control (historical) period spanning from 1986 to 2014, and three future periods: short-term (2025–2049), medium-term (2050–2074), and long-term (2075–2100).

Table 2. List of Regional Climate Models used in the study.

Global Circulation Models (GCMs) (Driver)	Regional Climate Model (RCM)	Country	Grid (Spatial Resolution)
Beijing Climate Center Climate System Model version 2, Model Resolution. (BCC-CSM2-MR)	Beijing Climate Center (BCC)	China	100 km
Community Earth System Model Version 2 (CESM2)	National Center for Atmospheric Research (NCAR)	USA	250 km
European Earth System Modelling Version 3 (EC-Earth3)	EC-Earth Consortium	Europe	250 km
Flexible Global Ocean-Atmosphere-Land System Model, version "g3" (FGOALS-g3)	Chinese Academy of Sciences (CAS)	China	250 km
Geophysical Fluid Dynamics Laboratory Earth System Model version 4 (GFDL-ESM4)	National Oceanic and Atmospheric Administration, Geophysical Fluid Dynamics Laboratory (NOAA-GFDL)	USA	100 km
Institute for Numerical Mathematics Coupled Model version 5 (INM-CM5)	Institute for Numerical Mathematics (INM)	Russia	100 km
Model for Interdisciplinary Research on Climate-Earth System Model, version 2, Low-resolution. (MIROC-ES2L)	JAMSTEC, AORI, NIES, and MIROC	Japan	500 km
Norwegian Earth System Model version 2—Medium resolution (NorESM2-MM)	NCC	Norway	100 km

3. Methodology

The methodologies followed in this research for updating the IDF curves by deriving climate change scenarios are presented in Figure 2. The process integrates observed precipitation data and Regional Climate Model (RCM) outputs to analyze extreme rainfall patterns. The data are downscaled using the Quantile Mapping (QM) method and then disaggregated using the K-nearest neighbor (KNN) method. Two goodness-of-fit (GoF) tests, namely the Kolmogorov-Smirnov (KS) and Chi-square (χ^2) tests, were used to check how well some theoretical distribution describes the disaggregated data. Extreme value modeling, using the Gumbel distribution, generates Intensity-Duration-Frequency (IDF) curves for both observed and future periods. These curves are then compared to assess how climate change may impact extreme precipitation events.

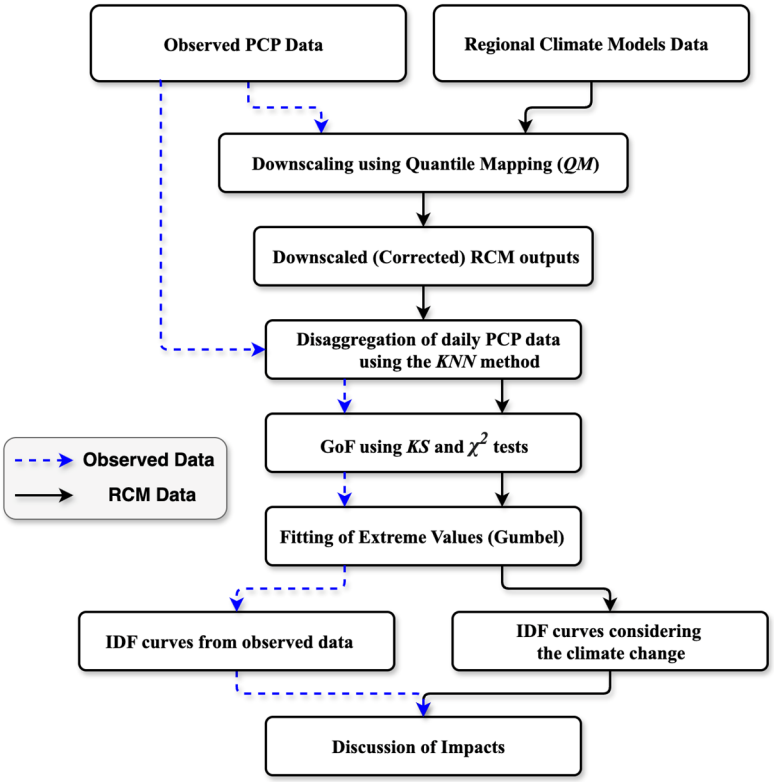


Figure 2. An illustrative flowchart delineating the methodologies for updating the IDF curves.

3.1. Extreme Values Analysis

3.1.1. Goodness of Fit Tests

The goodness of fit in a statistical model quantifies how well the model represents a set of observations. Generally, goodness-of-fit measures are applied to capture the difference between observed values and model predictions [39]. In this context, the Kolmogorov-Smirnov (KS) test and the Chi-Square (χ^2) test are employed to determine the best-fitting distribution for a dataset of annual maximum values.

Kolmogorov-Smirnov Test

The Kolmogorov-Smirnov test is a statistical tool that provides us with test statistics, enabling us to compare the goodness of fit among different distribution models. By analyzing the results of this test, the distribution that most closely matches the provided data can be identified [39]. Equation (1) illustrates the KS test.

$$\Delta = \ maximum\ of\ |P(x_i) - F(x_i)| \tag{1}$$

where Δ is the test statistic, $P(x_i)$ is the cumulative probability, and $F(x_i)$ is the theoretical cumulative. To accept the hypothesis that the assumed distribution is a good fit, the critical value of the Kolmogorov-Smirnov statistic Δ_o should be greater than the KS test statistic Δ [39].

Chi-Square Test

The chi-square goodness-of-fit test evaluates how well a theoretical distribution fits an empirical distribution. This test compares the observed sample distribution with the expected probability distribution. The sample data are divided into intervals, and the number of points in each interval is compared to the expected number of points based on

the hypothesized distribution [40]. The statistics of the chi-square goodness of fit test (χ^2) is computed as

$$\chi^2 = \sum \frac{(o_i - e_i)^2}{e_i} \quad (2)$$

where O_i is the observed frequencies, and e_i is the expected frequencies for the ith cell. To determine the critical region for a given level of significance α, the critical value α and the test statistic χ^2 are calculated. If $\alpha > \chi^2$, the null hypothesis (H_0) will be accepted [40].

3.1.2. The Gumbel Distribution

The Gumbel distribution, also known as the extreme value type 1 (EV1) distribution, is one of the most used PDFs for calculating extreme values in hydrological and meteorological studies [39]. For a hydrologic extreme event X, following Gumbel's distribution, the exceedance probability of $X = x_0$ is given by:

$$P(X \geq x_0) = 1 - e^{-e^{-(x-\beta)/\alpha}} \quad (3)$$

where α and β are the scale and location parameters of Gumbel's distribution, respectively. Following the procedure suggested by Maity [39], the return precipitation x_T (in mm) for each duration, based on a specified return period T (in years), is given by:

$$x_T = \overline{x} + K_T S_x \quad (4)$$

where S_x denotes the standard deviation, $\overline{x}$ is the mean. The Gumbel frequency factor (K_T) is computed as follows:

$$K_T = \frac{(y_T - \overline{y}_n)}{S_n} \quad (5)$$

where $\overline{y}_n$ is the reduced mean and S_n is the reduced standard deviation, both of which are functions of the record length n. For example, for the base period where (n = 30), the reduced mean ($\overline{y}_n$) is 0.5362, and the reduced standard deviation (S_n) is 1.1124 [41]. The reduced variate for the return period T, denoted as y_T, is calculated as follows:

$$y_T = -\left[ln\left(ln\frac{T}{T-1}\right)\right] \quad (6)$$

3.2. Statistical Downscaling for Bias Correction

Nonparametric Quantile Mapping Downscaling

The nonparametric quantile mapping (QM) approach offers a method for bias correction that does not rely on assumptions regarding the underlying data distribution. This approach ensures that regional climate model (RCM) future values align closely with observed data, reducing potential biases in the model's performance and enhancing the accuracy of climate modeling studies [42]. This technique employs the empirical Cumulative Distribution Function (ECDF), as outlined in Equation (7), which is derived from both observed and climate model data. These ECDFs play a critical role in estimating quantiles for bias correction. To accomplish bias correction, the process entails finding the nearest model output value from the base period that matches the desired future model output. Once this match is established, its corresponding ECDF value is assigned. This value is then linked to an observation value corresponding to the ECDF of the model output, resulting in the bias-corrected value. The following function is applied to produce the corrected future projections ($X_{corrected}$):

$$X_{corrected} = F_{OBS}^{-1}(F_{RCM}(x_{RCM})) \quad (7)$$

where F_{OBS} is the cumulative distribution function (CDF) of observations, $F_{OBS}{}^{-1}$ is the inverse CDF of the observed data, F_{RCM} is the cumulative distribution function for RCM data, and the mean change in the quantity of interest X_{RCM} [43].

3.3. Disaggregation Method

The K-nearest neighbor resampling (KNN) method, designed for generating hydrologic time series, was initially introduced by Lall and Sharma [44] and further developed by Taesam Lee et al. [42]. This study utilized an approach based on a K-nearest neighbor density estimator, employing the Euclidean distance to identify the Kth nearest data point and the corresponding volume encompassing K data points as presented in Figure 3.

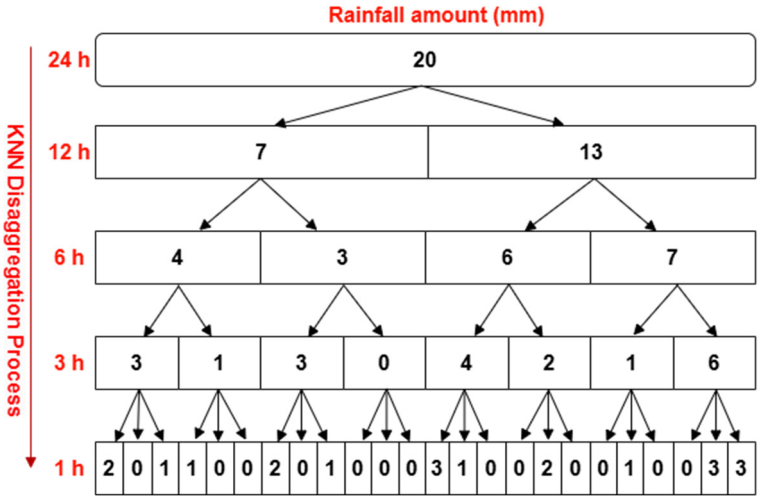


Figure 3. The K-nearest neighbor disaggregation process.

The KNN method selects a value from the observed dataset by evaluating the proximity between the given values and the observations of predictor variables, represented as a feature vector.

$$D_i = (X_t - x_i) - (X_t - x_i)^T \tag{8}$$

where D_i is the distance measured for (i = 1, . . ., n), X_t is the conditional feature vector (or a set of predictor variables at time t), and x_i is the corresponding observation vector. Through data calibration and validation, we compared selecting k randomly versus employing the closest k. With the large dataset, random selection often includes distant, less relevant points, reducing accuracy. In contrast, the closest k values are more representative and reliable, as shown through validation, making this approach more accurate and consistent for large datasets.

$$w_m = \frac{1/m}{\sum_{j=1}^{k} \frac{1}{j}}, m = 1, \ldots, k \tag{9}$$

where w_m is the Weight assigned to the m-th neighbor, m is the Index of the neighbor, k is the total number of nearest neighbors $k = \sqrt{n}$, and j is the summation index.

4. Results

4.1. Extreme Value Analysis for Observed Data

To determine the most appropriate distribution for predicting future precipitation based on the available observed data (1985–2001) of annual maximum values for durations of 10 (M10), 20 (M20), 30 (M30), 60 (H1), 120 (H2), 180 (H3), 360 (H6), 720 (H12), and 1440 (H24) minutes, several distributions were evaluated, including the Log-Pearson Type III, Weibull (3-parameter), Gumbel, Lognormal, and Normal distributions. A significance level (α) of 5% was applied in the analysis. As shown in Table 3, the results indicate that

the Gumbel distribution best fits the studied data. Consequently, the Gumbel distribution was selected to predict future precipitation. Previous studies in Saudi Arabia have recommended the use of the Gumbel distribution [17,19–21,45–47].

Table 3. Ranks of the best-fitted distributions on a scale from 1 (representing the best-fitting model) to 5 (denoting the least appropriate model).

	Gumbel		Log-Pearson 3		Lognormal		Normal		Weibull (3P)	
Duration	**K-S**	χ^2	**K-S**	χ^2	**K-S**	χ^2	**K-S**	χ^2	**K-S**	χ^2
M10	1	1	2	3	3	4	4	2	5	5
M20	1	3	1	1	2	4	4	5	3	2
M30	1	1	2	2	3	3	5	3	4	5
H01	2	1	5	5	2	2	3	4	1	3
H02	2	1	2	3	2	4	3	5	1	2
H03	1	5	1	4	2	2	2	1	3	3
H06	1	3	3	4	4	5	5	1	2	2
H12	2	2	2	3	1	4	4	1	3	5
H24	1	2	2	2	3	3	5	1	4	4

The critical values for the Kolmogorov-Smirnov (KS) and chi-square tests were 0.32 and 3.84, respectively. The *p*-values for the KS test ranged from 0.62 to 0.96, and for the chi-square test, they ranged from 0.37 to 0.90. Table 4 presents the parameters of the Gumbel distribution. Based on this best-fit model, return values for 2, 5, 10, 25, 50, and 100-year periods were calculated, as shown in Table 5. The IDF curves, derived from the observed precipitation datasets using the Gumbel distribution, are illustrated in Figure 4.

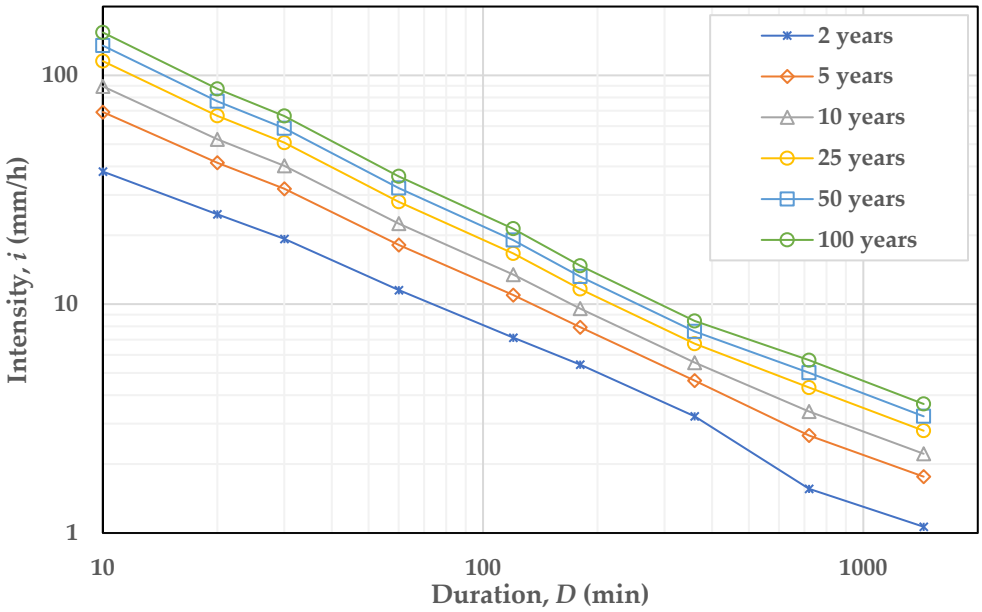


Figure 4. The IDF curves of Buridah station employing the Gumbel distribution.

Table 4. The parameters of the Gumbel distribution.

Parameters/Duration	**M10**	**M20**	**M30**	**H01**	**H02**	**H03**	**H06**	**H12**	**H24**
Location parameters	7.09	9.06	10.58	12.49	15.40	17.42	20.64	20.66	28.02
Scale parameters	5.09	5.49	6.20	6.49	7.49	7.32	8.23	13.04	16.4

Table 5. The return precipitation amounts (mm) using the Gumbel distribution.

Time (min)	Return Period (Years)					
	2	**5**	**10**	**25**	**50**	**100**
10	6.33	11.52	14.93	19.25	22.51	25.66
20	8.24	13.83	17.51	22.18	25.69	29.09
30	9.65	15.97	20.13	25.40	29.37	33.22
60	11.52	18.14	22.49	28.01	32.17	36.19
120	14.28	21.92	26.94	33.31	38.11	42.75
180	16.33	23.79	28.70	34.92	39.60	44.14
360	19.40	27.79	33.31	40.30	45.57	50.67
720	18.70	32.00	40.74	51.82	60.16	68.24
1440	25.56	42.29	53.27	67.21	77.71	87.87

4.2. Projected IDF Curves

The IDF curves were generated for the eight selected RCMs based on four SSPs and three future timeframes, as illustrated in Figure 5 and Table 6 for the Buraidah station. Generally, uncertainty in the IDF curves was more pronounced for high-emission scenarios and longer future periods, while it was lower for low-emission scenarios and shorter timeframes. The analysis also revealed a more significant increase in rainfall intensity for shorter durations compared to longer durations. For example, under SSP 8.5, using the CESM2 model at the Buraidah station, the 10-min rainfall intensity for a 2-year return period is projected to rise from 55.97 mm/hr to 61.96 mm/hr. In contrast, the 24-h intensity is expected to increase from 1.06 mm/hr to 1.54 mm/hr.

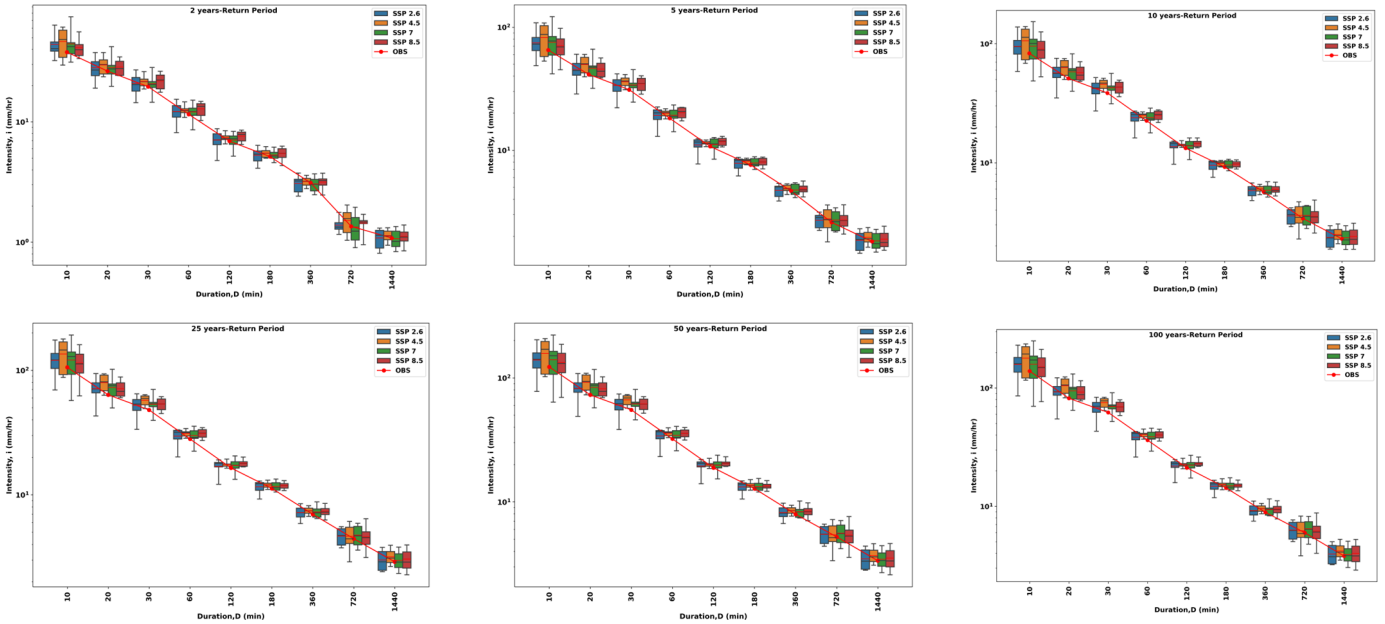
Tables 6 and 7 provide detailed changes in future rainfall intensities relative to the base period. The results for the Buraidah station indicate mean changes in the IDF curves ranging from 8.75% to 22.34% for 2025–2049, −0.52% to 8.25% for 2050–2074, and 6.07% to 15.43% for 2075–2099 compared to the base period. The mean changes for SSP 2.6 ranged from 8.75% to 10.63% during 2025–2049; for SSP 4.5, from 14.15% to 22.34%; for SSP 7.0, from 8.96% to 12.17%; and for SSP 8.5, from 9% to 9.85%. Across all scenarios, the most substantial changes were observed in the distant future (2075–2099). Specifically, the projected changes for SSP 2.6 ranged from 6.07% to 8.01%; for SSP 4.5, from 13.47% to 15.43%; for SSP 7.0, from 7.31% to 13.68%; and for SSP 8.5, from 12.95% to 13.75%. These results suggest that, while higher-emission scenarios (SSP 4.5, SSP 7.0, and SSP 8.5) are associated with more pronounced projected changes, the changes in lower-emission scenarios (SSP 2.6) tend to be smaller in the distant future (2075–2099) compared to the near future (2025–2049).

Figure 5 further illustrates a higher level of uncertainty in the projected changes in rainfall intensity for longer return periods across all scenarios and timeframes. For instance, for the 2-year return period, projected rainfall intensity changes range from 13.67 mm/hr to 14.35 mm/hr during 2025–2049, from 12.5 mm/hr to 12.96 mm/hr during 2050–2074, and from 13.33 mm/hr to 14.29 mm/hr during 2075–2099 across different SSPs. Conversely, for the 100-year return period, projected changes range from 45.6 mm/hr to 50.78 mm/hr during 2025–2049, from 42.18 mm/hr to 44.94 mm/hr during 2050–2074, and from 44.55 mm/hr to 47.92 mm/hr during 2075–2099.

A summary of the results for the whole station is presented in Table 7 and Figure 6. The differences between stations highlight the spatial variability in projected rainfall changes under various SSPs, time periods, and return durations. Buriydah exhibits consistent increases in rainfall across most SSPs, particularly in the far term (2075–2099), with SSP 8.5 showing notable extremes, signaling potential risks of intensified rainfall. Al Rass, however, displays a more erratic pattern, with negative changes in SSP 2.6 and substantial increases

under SSP 8.5, especially for shorter return periods in the far term, suggesting heightened variability. Badayea shows relatively modest changes, with negative trends under SSP 7 for longer durations in the mid-term but recovering to moderate increases by the far term under SSP 8.5. Al Mithnab experiences declines in earlier periods, particularly under SSP 7, but transitions to significant positive changes in the far term, reflecting increasing risks under higher emissions. Nabhaniyah stands out with the most extreme increases, particularly under SSP 8.5 for shorter return periods, underscoring its vulnerability to future climate extremes. In contrast, Unaizah shows smaller magnitudes of change, with negative trends under SSP 7 and only slight rebounds under SSP 8.5, indicating relatively stable conditions compared to other stations.

(**a**) Future short period for Buraidah Station



(**b**) Future medium period for Buraidah station

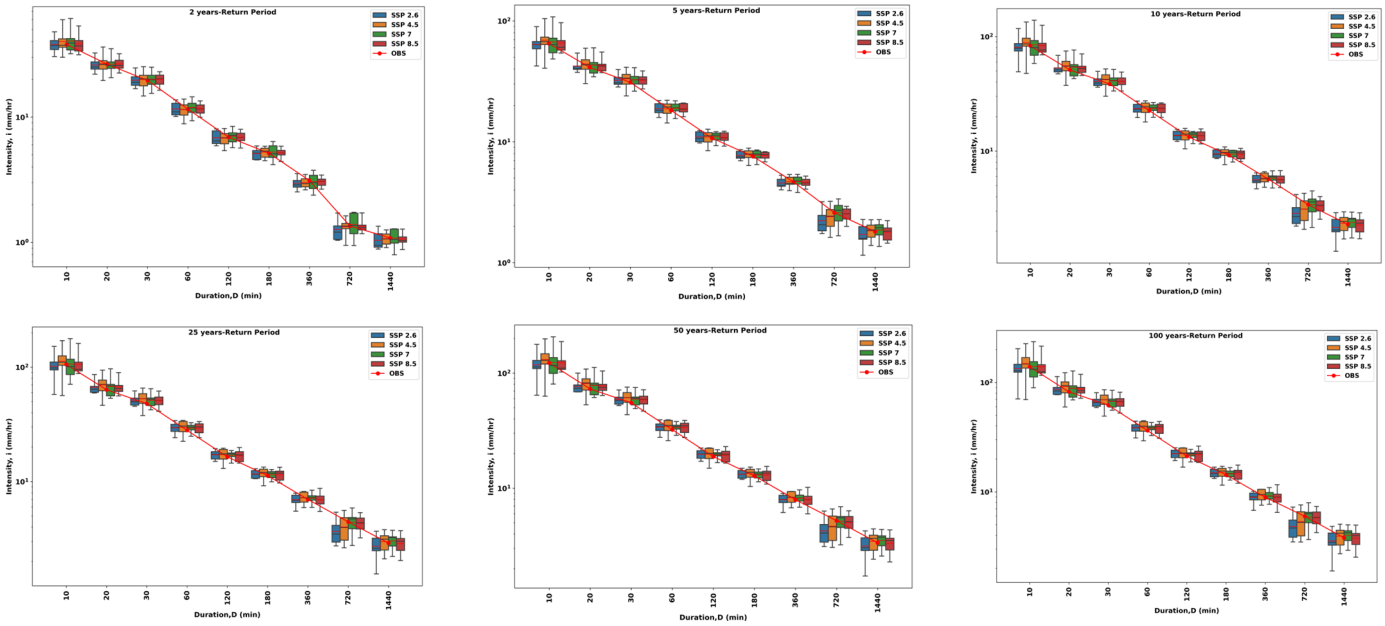


Figure 5. *Cont.*

(**c**) Future long period for Buraidah station

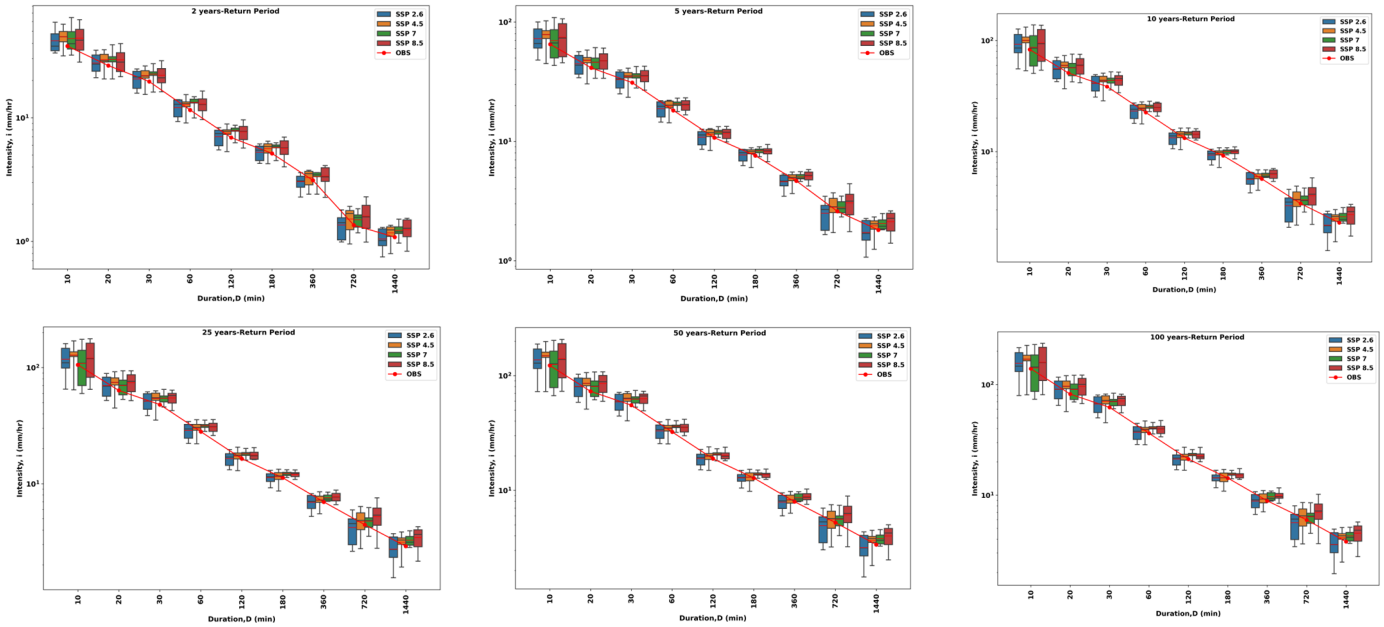


Figure 5. The IDF curves developed for all eight RCMs across four SSPs (boxplots) and the observed IDF curves (red lines) for (**a**) short-term, (**b**) mid-term, and (**c**) long-term future periods of Buraidah station.

Table 6. Projected Mean rainfall returns values in three future periods and four SSPs for different durations of Buraidah station.

		2025–2049				**2050–2074**				**2075–2099**			
Model	**T**	**2.6**	**4.5**	**7**	**8.5**	**2.6**	**4.5**	**7**	**8.5**	**2.6**	**4.5**	**7**	**8.5**
BCC-CSM2	2	12.03	11.66	12.06	11.69	11.21	9.76	10.20	10.90	11.89	10.05	13.11	10.41
	5	20.88	19.39	19.34	19.19	18.73	14.60	17.29	18.28	19.52	14.87	19.12	16.42
	10	26.75	24.53	24.17	24.17	23.71	17.81	21.99	23.18	24.58	18.07	23.11	20.41
	25	34.07	30.92	30.19	30.37	29.93	21.81	27.84	29.28	30.89	22.05	28.08	25.38
	50	39.60	35.76	34.75	35.06	34.63	24.84	32.27	33.89	35.66	25.07	31.84	29.14
	100	45.04	40.52	39.23	39.68	39.25	27.81	36.63	38.44	40.36	28.03	35.54	32.84
CESM2	2	18.06	15.93	20.18	16.62	13.01	17.27	17.42	15.51	17.02	16.78	18.49	19.02
	5	29.24	27.76	32.06	27.16	20.01	28.84	29.04	26.56	27.64	27.88	29.62	29.41
	10	36.66	35.60	39.94	34.16	24.66	36.52	36.74	33.90	34.69	35.25	37.01	36.30
	25	45.90	45.39	49.76	42.88	30.45	46.10	46.35	43.04	43.48	44.43	46.22	44.89
	50	52.88	52.78	57.18	49.46	34.82	53.33	53.61	49.95	50.12	51.37	53.18	51.38
	100	59.76	60.06	64.49	55.95	39.13	60.46	60.76	56.76	56.66	58.20	60.03	57.77
EC-Earth3	2	13.69	11.64	12.09	13.20	12.05	12.03	12.34	12.03	13.01	12.64	13.64	11.32
	5	22.68	20.21	18.92	19.78	18.49	21.59	20.47	20.48	22.34	23.12	20.13	20.39
	10	28.64	25.90	23.46	24.14	22.76	27.94	25.86	26.09	28.53	30.07	24.44	26.41
	25	36.07	32.99	29.10	29.58	28.09	35.86	32.58	33.08	36.24	38.74	29.81	33.90
	50	41.69	38.35	33.38	33.69	32.11	41.84	37.66	38.36	42.07	45.28	33.87	39.57
	100	47.22	43.63	37.58	37.74	36.08	47.72	42.67	43.56	47.81	51.73	37.86	45.15

Table 6. *Cont.*

		2025–2049				2050–2074				2075–2099			
Model	**T**	**2.6**	**4.5**	**7**	**8.5**	**2.6**	**4.5**	**7**	**8.5**	**2.6**	**4.5**	**7**	**8.5**
FGOALS-g3	2	14.19	17.86	13.14	14.73	13.72	12.92	12.57	14.14	15.19	17.30	15.01	18.18
	5	23.82	29.12	23.10	24.14	22.21	22.81	18.60	22.67	25.17	28.27	24.77	29.40
	10	30.21	36.58	29.71	30.39	27.84	29.36	22.61	28.33	31.80	35.55	31.25	36.84
	25	38.17	45.88	37.95	38.17	34.87	37.53	27.60	35.38	40.05	44.62	39.32	46.11
	50	44.19	52.92	44.17	44.05	40.17	43.71	31.37	40.71	46.29	51.47	45.42	53.12
	100	50.11	59.84	50.30	49.84	45.40	49.79	35.08	45.95	52.43	58.22	51.43	60.02
GFDL-ESM4	2	9.70	13.96	10.17	12.09	11.94	12.42	10.68	12.16	10.57	14.11	10.82	12.60
	5	14.86	22.91	16.44	19.49	19.22	20.12	16.62	20.16	17.32	22.48	18.27	20.17
	10	18.29	28.85	20.60	24.40	24.06	25.22	20.56	25.48	21.79	28.03	23.21	25.19
	25	22.56	36.25	25.79	30.52	30.08	31.58	25.47	32.10	27.37	34.95	29.37	31.45
	50	25.79	41.84	29.71	35.15	34.63	36.39	29.18	37.10	31.59	40.18	34.03	36.19
	100	28.97	47.35	33.57	39.70	39.11	41.12	32.84	42.03	35.75	45.33	38.61	40.84
INM-CM5	2	17.46	11.69	14.66	11.53	15.43	12.69	14.72	13.46	12.53	15.18	13.75	15.16
	5	27.62	19.24	24.08	19.04	26.22	19.85	22.54	20.79	17.62	23.60	19.28	24.98
	10	34.36	24.25	30.34	24.02	33.38	24.60	27.73	25.66	21.00	29.19	22.95	31.50
	25	42.76	30.49	38.14	30.23	42.30	30.52	34.19	31.72	25.21	36.15	27.52	39.62
	50	49.11	35.21	44.03	34.92	49.05	34.99	39.08	36.31	28.39	41.42	30.98	45.76
	100	55.36	39.85	49.83	39.54	55.69	39.40	43.89	40.82	31.53	46.60	34.39	51.80
MIROC-ES2L	2	12.19	16.91	14.26	13.56	12.20	11.30	12.74	12.02	10.61	13.95	15.41	15.23
	5	21.03	27.90	23.73	22.58	19.87	19.74	22.23	18.54	17.89	22.45	24.47	26.04
	10	26.90	35.19	30.02	28.57	24.96	25.35	28.53	22.87	22.72	28.09	30.48	33.21
	25	34.21	44.27	37.85	36.03	31.30	32.33	36.38	28.27	28.74	35.12	37.98	42.15
	50	39.73	51.14	43.77	41.67	36.10	37.61	42.31	32.34	33.29	40.44	43.64	48.90
	100	45.17	57.90	49.60	47.22	40.82	42.81	48.15	36.36	37.76	45.67	49.22	55.55
NorESM2-MM	2	12.05	15.14	13.02	16.18	10.49	14.25	13.01	11.28	15.86	14.10	14.09	11.66
	5	18.40	26.40	22.38	26.62	18.93	23.94	21.73	18.82	26.80	23.60	23.53	17.59
	10	22.61	33.86	28.58	33.54	24.53	30.36	27.51	23.83	34.06	29.91	29.79	21.52
	25	27.86	43.17	36.32	42.17	31.51	38.37	34.72	30.07	43.11	37.78	37.60	26.43
	50	31.83	50.20	42.16	48.70	36.79	44.43	40.16	34.78	49.95	43.72	43.50	30.14
	100	35.73	57.12	47.92	55.12	41.98	50.39	45.53	39.42	56.69	49.57	49.30	33.78

Table 7. The mean projected changes (%) in rainfall return periods for all stations, covering different models over different SSPs and three future periods, relative to the base period.

Station	**T**	**2025–2049**				**2050–2074**				**2075–2099**			
		SSP 2.6	**SSP 4.5**	**SSP 7**	**SSP 8.5**	**SSP 2.6**	**SSP 4.5**	**SSP 7**	**SSP 8.5**	**SSP 2.6**	**SSP 4.5**	**SSP 7**	**SSP 8.5**
Buriydah	2	8.75	14.15	8.96	9.00	−0.52	2.05	3.10	0.92	6.07	13.47	13.68	12.95
	5	9.72	18.56	10.66	9.40	0.59	5.39	3.56	2.21	7.12	14.48	10.14	13.33
	10	10.26	20.25	11.44	9.76	1.16	6.70	3.92	2.84	7.68	15.05	9.20	13.68
	25	10.29	21.16	11.66	9.65	1.25	7.35	3.84	2.98	7.75	15.08	8.06	13.55
	50	10.36	21.70	11.83	9.64	1.35	7.75	3.85	3.10	7.83	15.16	7.52	13.54
	100	10.63	22.34	12.17	9.85	1.62	8.25	4.05	3.38	8.10	15.43	7.31	13.75
Al Rass	2	2.47	5.15	6.05	15.50	−1.78	10.22	7.25	14.17	0.97	19.41	16.53	19.68
	5	0.51	−0.87	1.44	9.65	−4.57	4.52	1.84	6.79	−1.20	10.68	8.61	12.72
	10	0.18	−2.37	0.36	8.23	−5.15	3.13	0.53	4.93	−1.59	8.44	6.61	10.99
	25	−0.46	−3.87	−0.84	6.75	−5.95	1.69	−0.85	3.12	−2.27	6.34	4.68	9.26
	50	−0.72	−4.57	−1.39	6.06	−6.30	1.02	−1.48	2.27	−2.56	5.34	3.77	8.45
	100	−0.72	−4.90	−1.60	5.76	−6.38	0.72	−1.76	1.84	−2.58	4.82	3.31	8.06

Table 7. *Cont.*

Station	T	2025–2049				2050–2074				2075–2099			
		SSP 2.6	SSP 4.5	SSP 7	SSP 8.5	SSP 2.6	SSP 4.5	SSP 7	SSP 8.5	SSP 2.6	SSP 4.5	SSP 7	SSP 8.5
Al Badayea	2	3.06	9.23	1.05	3.75	4.98	2.09	0.64	4.35	5.59	10.95	10.34	9.49
	5	3.08	8.07	−3.92	0.84	4.63	−1.74	−2.93	−2.33	4.34	6.11	8.17	8.29
	10	3.29	7.89	−5.40	0.06	4.72	−2.83	−3.93	−4.38	4.13	4.70	7.66	8.10
	25	3.10	7.38	−6.91	−0.91	4.43	−4.04	−5.07	−6.35	3.60	3.20	6.87	7.57
	50	3.05	7.16	−7.66	−1.37	4.32	−4.64	−5.62	−7.35	3.37	2.46	6.51	7.35
	100	3.20	7.19	−8.06	−1.54	4.44	−4.91	−5.87	−7.93	3.38	2.09	6.43	7.37
Al Mithnab	2	1.85	9.91	−1.52	3.96	−5.57	−0.53	−3.72	3.85	4.42	6.79	11.57	5.56
	5	7.51	14.20	8.14	7.99	−3.43	3.25	4.62	13.91	5.91	10.11	19.28	11.88
	10	9.53	15.80	11.45	9.50	−2.55	4.68	7.50	17.36	6.60	11.40	21.99	14.13
	25	10.73	16.64	13.64	10.29	−2.21	5.41	9.37	19.64	6.76	12.00	23.67	15.47
	50	11.40	17.14	14.83	10.75	−1.98	5.85	10.39	20.88	6.90	12.37	24.60	16.23
	100	12.12	17.73	15.95	11.31	−1.63	6.37	11.37	22.05	7.20	12.87	25.54	17.03
Al Nabhaniyah	2	11.04	15.81	12.32	25.59	11.68	14.94	11.09	14.18	13.98	18.47	28.62	19.52
	5	3.50	7.52	8.87	17.82	4.71	6.27	4.51	5.28	3.37	8.32	18.61	12.18
	10	1.56	5.37	8.12	15.84	2.94	4.01	2.85	2.96	0.55	5.65	15.99	10.32
	25	−0.29	3.35	7.14	13.91	1.20	1.91	1.20	0.81	−1.96	3.23	13.58	8.50
	50	−1.17	2.39	6.71	13.00	0.38	0.90	0.43	−0.21	−3.18	2.06	12.42	7.64
	100	−1.63	1.88	6.59	12.55	−0.02	0.36	0.05	−0.78	−3.88	1.40	11.79	7.21
Onaizah	2	0.20	2.55	−3.19	8.65	2.19	1.58	−4.27	−0.19	0.09	6.97	8.10	0.83
	5	0.60	2.68	−1.52	7.96	3.15	1.91	−4.76	−0.15	−0.97	5.87	5.14	1.96
	10	0.93	2.93	−0.78	7.95	3.68	2.22	−4.73	0.06	−1.12	5.72	4.37	2.53
	25	0.84	2.76	−0.54	7.56	3.73	2.11	−5.04	−0.13	−1.59	5.23	3.39	2.63
	50	0.84	2.72	−0.36	7.41	3.80	2.10	−5.16	−0.18	−1.78	5.03	2.93	2.73
	100	1.03	2.89	−0.04	7.50	4.06	2.29	−5.07	−0.03	−1.75	5.07	2.78	2.99

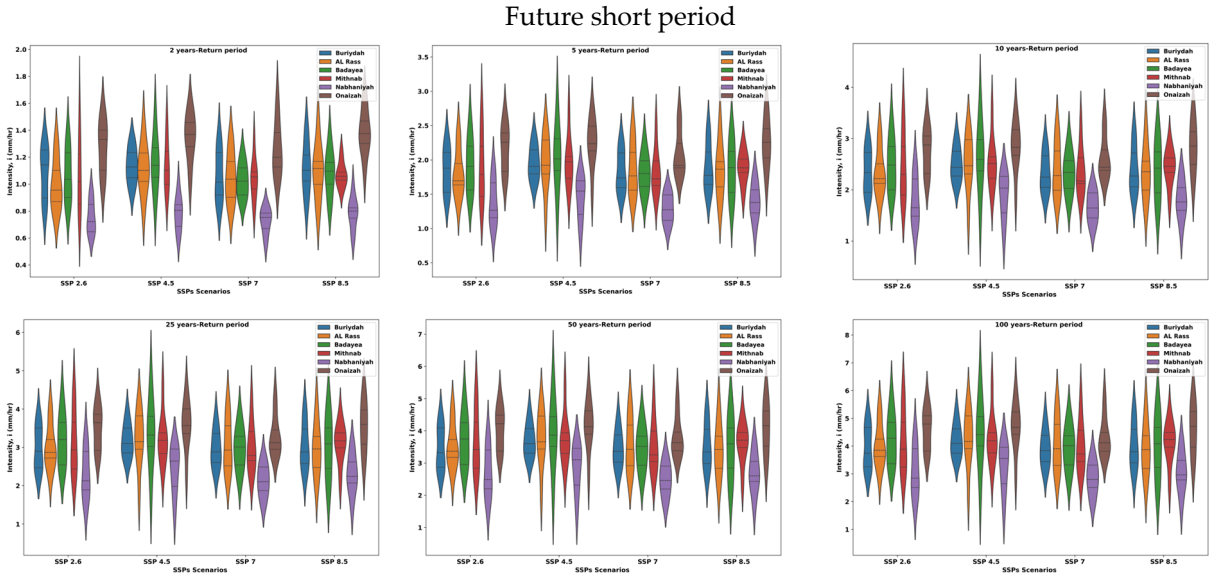


Figure 6. *Cont.*

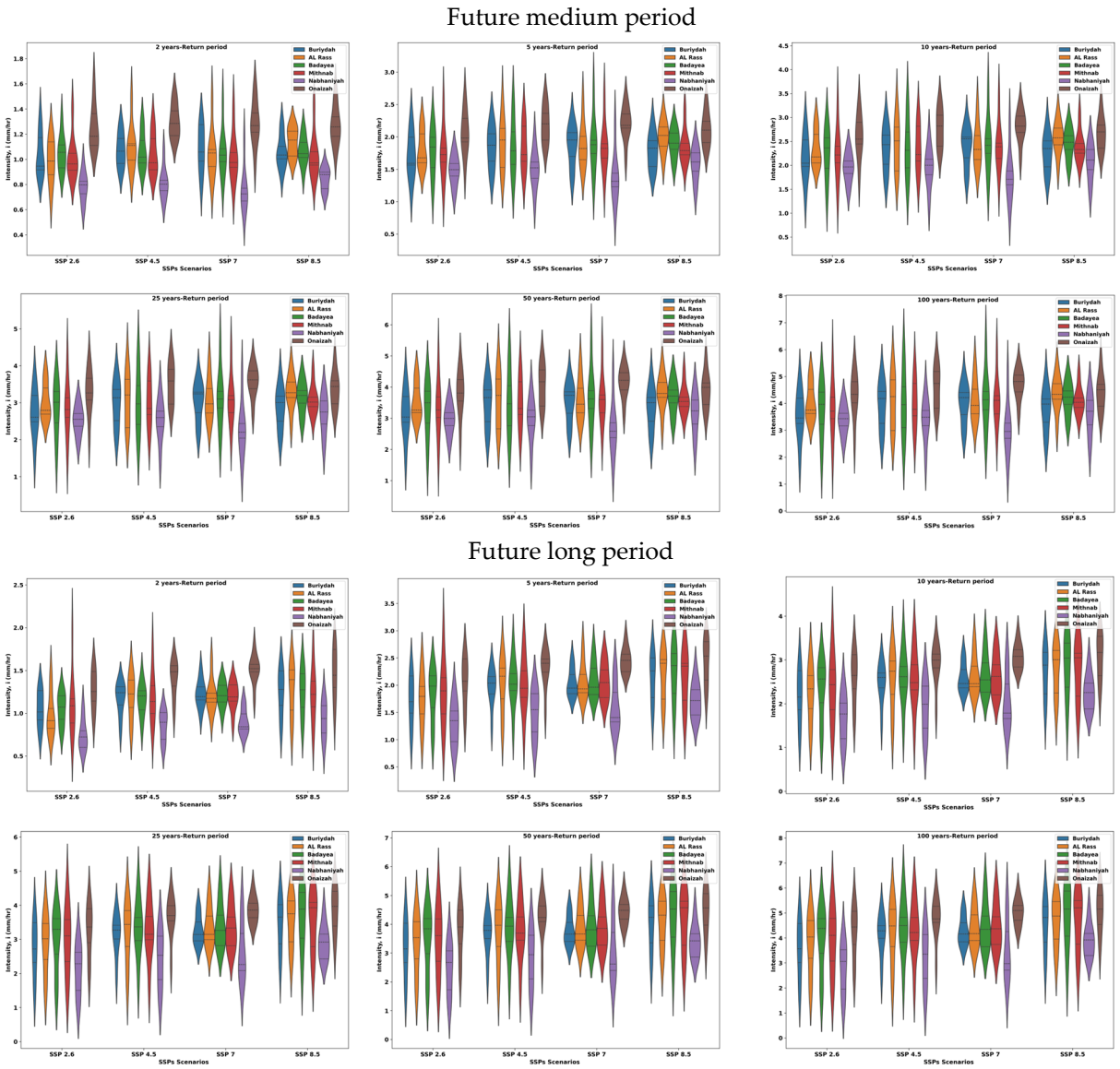


Figure 6. Violin plots of the projected annual maximum precipitation intensity for all stations for comparison, covering different models and SSPs for three future periods. Tthe dotted lines represent the 25th percentile (Q1), the 50th percentile (median), and the 75th percentile (Q3) of the data distribution.

5. Discussion

In this study, the Gumbel distribution was used after comparing several distributions. These outcomes indicate that the Gumbel distribution is the best fit for the studied data, a finding also reported by several studies across the region. For instance, Ewea et al. [17] found that the Gumbel Type I distribution was the most suitable for the Makkah Al Mukarramah region. Also, Elsebaie et al. [19] compared the log-Pearson Type III and Gumbel distributions for the Wadi AL-Lith region and found that the former produced slightly better results. Kawara and Elsebaie [20] determined that the Log-Pearson Type III and Gumbel distributions fit the available data in the Yalamlam Area. Al-Amri and Subyani [21] applied the Log-Pearson Type III and Gumbel distributions to a station in Al-Madinah city and recommended the latter for ungauged sites in the arid region of Al-Madinah city. However, Subyani and Al-Amri [44] found no remarkable difference between the Gumbel and LPT III methods for Al-Madinah city. Ewea et al. [46] used the Gumbel distribution method to obtain the parameters for the IDF formula for KSA as a

whole. Similarly, Elsebaie [47] determined that the Gumbel distribution produced slightly higher results than the LPT III distribution for some regions, including a station in the Qassim region.

In the present study, historical data from eight RCMs underestimated the observed data, highlighting the necessity for bias correction methods. The underestimation of intense precipitation has led to satellite precipitation data underestimating IDF curves, as demonstrated by several studies [48–50]. This issue is particularly significant in many cases. For example, Yan et al. [48] reported a nearly 70% underestimation of observed IDF curves in Singapore using GSMaP, while Ombadi et al. [49] found underestimations of 3% and 22% in the U.S. using satellite rainfall-based IDF curves. Noor et al. [50] demonstrated underestimations ranging from 16% to 54% using GSMaP_GC, 8% to 12% for return periods (RPs) greater than 10 years, and 36% to 54% for RPs below 10 years. In this study, the negative results presented in Table 7 indicate consistent underestimations of return periods, particularly for longer durations (50 and 100 years) under SSP 2.6, SSP 4.5, and SSP 7.0 scenarios. These underestimations are more pronounced during the medium-term (2050–2074) and far-future (2075–2099) periods. For instance, in Al Rass, the 50- and 100-year return periods under SSP 2.6 in the medium-term were underestimated by −6.30% and −6.38%, respectively, while similar trends persisted in the long-future with deviations of −2.56% and −2.58%. This study utilized all available regional climate models (RCMs) included in CMIP6 and employed ensemble modeling to minimize biases associated with individual models. However, uncertainties within the models and limitations in grid resolution present challenges that could influence our climate change analysis and impact the reliability of the results.

The estimates revealed that rainfall intensities generally increased with the return period but decreased as rainfall duration increased across all stations [51]. Zhu et al. [52] reported a more substantial increase in magnitude at more extended return periods, while the percentage increase remained relatively similar across most return periods. The studies also suggested a more remarkable rise in extreme values under higher emission scenarios over extended periods. Therefore, the elevation of IDF curves in this study is warranted, and the findings also showed higher IDF curves for more intense RCPs [53]. The present study suggests that higher emission scenarios (SSP 4.5, SSP 7.0, and SSP 8.5) for a longer future period show greater projected changes compared to a shorter future period.

The projected mean annual precipitation for the 2020s indicates a 5%, 5.4%, and 5% decrease under the RCP2.6, RCP4.5, and RCP8.5 scenarios, respectively. By the 2080s, precipitation will decrease by 5.9% under RCP2.6 and 5.6% under RCP4.5. For the most extreme scenario (RCP8.5), future rainfall is expected to decline by 5.9% at the stations studied [54]. In the present study, the mean precipitation change at Buraidah station for the short-term future period under SSP 2.6 is 10%, SSP 4.5 is 19.69%, SSP 7 is 11.12%, and SSP 8.5 is 9.85%, considering various models, durations, and return periods. For the long-term future, the mean precipitation change is projected to be 7.43% under SSP 2.6, 14.78% under SSP 4.5, 9.32% under SSP 7, and 13.47% under SSP 8.5. However, based on the climate change report by IPCC 2007 [55], the high-risk scenario and corresponding numerical value are recommended for any design work.

Regionally, Buraidah is anticipated to experience consistent increases in rainfall, particularly under SSP 8.5 in the far term (2075–2099), indicating a potential escalation in extreme precipitation events. This pattern aligns with findings from a study by Almazroui et al. [1], which reported that the Arabian Peninsula is projected to experience a 12% to 107% increase in annual-averaged precipitation under high emission scenarios in the far future. Similarly, Nabhaniyah is projected to face substantial rainfall increases under SSP 8.5 for shorter return periods, underscoring its vulnerability to future climate extremes. In

contrast, stations like Al Rass and Al Mithnab exhibit more erratic patterns, with both negative and positive changes depending on the SSP and time, reflecting heightened variability. These observations are consistent with research indicating that precipitation variability is projected to widen, particularly after 2030, varying as much as 60% annually from one year to the next, thereby raising the risk of both droughts and floods [56]. This represents a notable departure from findings in the historical record, where analyses revealed no statistically significant trends in annual maximum precipitation [57], highlighting a potential shift in climatic patterns that may result in increased extremes.

In conclusion, the findings of this study are significantly affected by the specific model employed, as different models produced varied results due to differences in assumptions, structure, and inputs. Also, climate models are typically run under different scenarios of future emissions and societal development, leading to a range of potential outcomes. Therefore, the numerical values presented should be viewed as relative indicators rather than absolute predictions, offering insights into potential future climate impacts. This highlights the importance of considering multiple models and scenarios to capture a broad spectrum of possible futures, which is essential for making informed, flexible decisions in planning and policy that can adapt to the uncertainties inherent in long-term climate projections. Despite the uncertainties inherent in climate projections, it is crucial not to overlook the potential impacts of climate change on the generation of IDF curves, as changes in rainfall patterns could lead to more frequent and severe risks for infrastructure in the future [58,59]. One of the limitations of this study was the availability of sufficiently long and high-quality precipitation data, which is widely utilized in climate studies to establish baseline conditions. Previous studies have commonly used 30 years of data to analyze climate change trends. For instance, Q. Y. et al. [5] used the reference period from 1986 to 2005. Additionally, Mesgaria et al. [11], Noor et al. [51], and Almazroui et al. [1] also adopted a 30-year base period in their analyses. Furthermore, the integration of additional climatic factors into future research is warranted to facilitate a more comprehensive understanding of their interactions and impacts on hydrological systems.

6. Conclusions

This study comprehensively analyzes the Intensity-Duration-Frequency (IDF) curves for the Wadi Al Rummah region in the Qassim region in the context of climate change. It provides valuable insights into how future precipitation patterns may evolve under different SSPs utilizing observed data from several meteorological stations and downscaled outputs from eight Regional Climate Models (RCMs) within the CMIP6 framework. The Gumbel distribution was robust in modeling extreme precipitation events in the region, and the downscaling methods highlighted the necessity of bias correction to align model projections with observed data.

The results indicate significant changes in rainfall intensities, particularly for short-duration, high-frequency events, with notable increases in intensity under higher emission scenarios (SSP 4.5, SSP 7.0 and SSP 8.5). Future projections suggest that while rainfall intensity is expected to increase in all scenarios, the magnitude of these changes is most pronounced under high-emission scenarios and over the long-term period (2075–2100). Specifically, under SSP 8.5, substantial increases in rainfall intensity are observed for shorter durations, such as the 10-min rainfall intensity rising from 55.97 mm/hr to 61.96 mm/hr for a 2-year return period, while longer durations show more modest changes, such as the 24-h intensity increasing from 1.06 mm/hr to 1.54 mm/hr. For SSP 2.6, changes are generally smaller and tend to diminish in the far future (2075–2099) compared to the near future (2025–2049), reflecting a lower magnitude of projected risks. For SSP 4.5 and SSP 7.0, rainfall intensities exhibit moderate to substantial increases, with the largest changes occurring

in the distant future, particularly for shorter return periods. The IDF curve uncertainty was more pronounced for high-emission scenarios and longer timeframes, with substantial variability noted for higher return periods (e.g., the 100-year return period).

The station-specific analysis highlights spatial variability in rainfall changes, where Buraidah consistently shows increases across all SSPs, particularly under SSP 8.5 in the far-term, signaling potential risks of intensified rainfall. Al Rass displays erratic changes, with negative trends in SSP 2.6 and significant increases under SSP 8.5, particularly for short return periods, reflecting heightened variability. Badayea experiences modest changes, with declines under SSP 7.0 in the mid-term but recovering to moderate increases under SSP 8.5 in the far-term. Al Mithnab shifts from earlier declines under SSP 7.0 to notable positive changes in the far-term, highlighting the increasing risks under higher emissions. Nabhaniyah demonstrates the most extreme increases in rainfall, particularly under SSP 8.5 for short return periods, underscoring its vulnerability to climate extremes, while Unaizah remains relatively stable, with slight changes under SSP 8.5 and a more muted response overall. These results emphasize the varying implications of each SSP, where SSP 8.5 poses the greatest risks with intensified rainfall and increased uncertainty, while SSP 2.6 presents smaller, more stable changes, particularly in the distant future. The intermediate scenarios (SSP 4.5 and SSP 7.0) indicate moderate risks, suggesting the need for cautious long-term adaptation strategies.

This study underscores the critical need for updating IDF curves to reflect changing precipitation patterns, informing the design of climate-resilient infrastructure—particularly in arid regions such as the Qassim area. Future infrastructure planning and water resource management must incorporate these projected changes to ensure sustainability and reduce vulnerability to climate-induced risks. The results also highlight the importance of adopting region-specific climate adaptation strategies to mitigate the adverse effects of climate change, particularly in areas susceptible to shifts in precipitation dynamics. This study highlighted the importance of considering multiple climate models and scenarios to account for uncertainties in future climate projections and their impact on infrastructure risks. The findings of this study are relevant to other arid regions, which face similar risks of extreme rainfall events and flash floods due to climate change. By adopting similar methodologies and updating IDF curves, these regions can better prepare for future precipitation shifts and improve infrastructure resilience. Policymakers and practitioners should prioritize updating IDF curves for urban infrastructure design, focusing on high-risk areas like Buraidah and Nabhaniyah under SSP 8.5. Flexible, multi-scenario adaptation strategies must guide development to address both near- and long-term changes. Nature-based solutions, including green infrastructure, floodplains, and retention systems, should be integrated to enhance water retention, reduce runoff, and improve resilience. Accurate climate projections using bias correction like IDF_CC tools are crucial for reliable infrastructure planning. Strengthening early warning systems, building stakeholder capacity, and securing robust funding mechanisms are essential to mitigate extreme rainfall and flash flood risks. These measures will support sustainable and resilient infrastructure development in arid regions like Qassim.

Author Contributions: Conceptualization, A.A.; methodology, A.A. and M.A.; software, M.A.; validation, A.A. and M.A.; formal analysis, A.A. and M.A.; investigation, A.A. and M.A.; resources, A.A.; data curation, A.A. and M.A.; writing—original draft preparation, M.A.; writing—review and editing, A.A.; visualization, A.A. and M.A.; supervision, A.A.; project administration, A.A.; funding acquisition, A.A. All authors have read and agreed to the published version of the manuscript.

Funding: The authors gratefully acknowledge Qassim University, represented by the Deanship of Scientific Research, on the financial support for this research under the number (2023-SDG-1-BSRC36462) during the academic year 1445 AH/2023 AD.

Institutional Review Board Statement: Not applicable.

Informed Consent Statement: Not applicable.

Data Availability Statement: All relevant data are included in the paper.

Acknowledgments: The authors would like to thank Qassim University, represented by the Deanship of Graduate Studies and Scientific Research, for funding this research (2023-SDG-1-BSRC36462).

Conflicts of Interest: The authors declare no conflicts of interest.

References

1. Almazroui, M.; Islam, M.N.; Saeed, S.; Saeed, F.; Ismail, M. Future Changes in Climate over the Arabian Peninsula based on CMIP6 Multimodel Simulations. *Earth Syst. Environ.* **2020**, *4*, 611–630. [CrossRef]
2. IPCC. *Global Warming of 1.5 °C*; Cambridge University Press: Cambridge, UK, 2018. [CrossRef]
3. NASA. What Is Climate Change? | Facts–Climate Change: Vital Signs of the Planet. Available online: https://climate.nasa.gov/what-is-climate-change/ (accessed on 22 August 2023).
4. Allan, R.P.; Arias, P.A.; Berger, S.; Canadell, J.G.; Cassou, C.; Chen, D.; Cherchi, A.; Connors, S.L.; Coppola, E.; Cruz, F.A.; et al. Intergovernmental Panel on Climate Change (IPCC). Summary for Policymakers. In *Climate Change 2021: The Physical Science Basis*; Contribution of Working Group I to the Sixth Assessment Report of the Intergovernmental Panel on Climate Change; Cambridge University Press: Cambridge, UK, 2023; pp. 3–32.
5. Tarawneh, Q.Y.; Chowdhury, S. Trends of climate change in Saudi Arabia: Implications on water resources. *Climate* **2018**, *6*, 8. [CrossRef]
6. IPCC. *Intergovernmental Panel on Climate Change: IPCC (2023) Climate Change 2023, Synthesis Report (AR6)*; IPCC: Geneva, Switzerland, 2023. [CrossRef]
7. NASA. How Does Climate Change Affect Precipitation? | NASA Global Precipitation Measurement Mission. Available online: https://gpm.nasa.gov/resources/faq/how-does-climate-change-affect-precipitation (accessed on 27 August 2023).
8. Alodah, A. Towards Sustainable Water Resources Management Considering Climate Change in the Case of Saudi Arabia. *Sustainability* **2023**, *15*, 14674. [CrossRef]
9. Almazroui, M.; Saeed, S.; Saeed, F.; Islam, M.N.; Ismail, M. Projections of Precipitation and Temperature over the South Asian Countries in CMIP6. *Earth Syst. Environ.* **2020**, *4*, 297–320. [CrossRef]
10. Hejazizadeh, Z.; Hosseini, S.A.; Karbalaee, A.; Barabadi, R.P.; Mousavi, S.M. Spatiotemporal variations in precipitation extremes based on CMIP6 models and Shared Socioeconomic Pathway (SSP) scenarios over MENA. *Arab. J. Geosci.* **2022**, *15*, 1601. [CrossRef]
11. Mesgari, E.; Hosseini, S.A.; Partoo, L.G.; Hemmesy, M.S.; Houshyar, M. Assessment of CMIP6 models' performances and projection of precipitation based on SSP scenarios over the MENAP region. *J. Water Clim. Change* **2022**, *13*, 3607–3619. [CrossRef]
12. Kotwicki, V.; Al Sulaimani, Z. Climates of the Arabian Peninsula—Past, present, future. *Int. J. Clim. Change Strateg. Manag.* **2009**, *1*, 297–310. [CrossRef]
13. Majdi, F.; Hosseini, S.A.; Karbalaee, A.; Kaseri, M.; Marjanian, S. Future projection of precipitation and temperature changes in the Middle East and North Africa (MENA) region based on CMIP6. *ThApC* **2022**, *147*, 1249–1262. [CrossRef]
14. Wilby, R.L.; Charles, S.P.; Zorita, E.; Timbal, B.; Whetton, P.; Mearns, L.O. Guidelines for Use of Climate Scenarios Developed from Statistical Downscaling Methods Document history. 2004. Available online: https://www.researchgate.net/publication/200472164 (accessed on 30 August 2023).
15. UNFCCC. Dynamical Downscaling. Available online: https://unfccc.int/files/adaptation/methodologies_for/vulnerability_and_adaptation/application/pdf/dynamical_downscaling.pdf (accessed on 30 August 2023).
16. UNFCCC. Downscaling of Climate Model Projections | Climate Technology Centre & Network | Tue, 11/08/2016. Available online: https://www.ctc-n.org/technologies/downscaling-climate-model-projections (accessed on 30 August 2023).
17. Ewea, H.A.; Elfeki, A.M.; Bahrawi, J.A.; Al-Amri, N.S. Modeling of IDF curves for stormwater design in Makkah Al Mukarramah region, the Kingdom of Saudi Arabia. *Open Geosci.* **2018**, *10*, 954–969. [CrossRef]
18. Awadallah, A.G. Regional intensity-duration-frequency curves for Jeddah region, Saudi Arabia, using ordinary and L-moments approaches. *J. Flood Risk Manag.* **2015**, *8*, 195–207. [CrossRef]
19. Elsebaie, I.H.; El Alfy, M.; Kawara, A.Q. Spatiotemporal variability of intensity–duration–frequency (Idf) curves in arid areas: Wadi Al-Lith, Saudi Arabia as a case study. *Hydrology* **2022**, *9*, 6. [CrossRef]
20. Kawara, A.Q.; Elsebaie, I.H. Development of Rainfall Intensity, Duration and Frequency Relationship on a Daily and Sub-Daily Basis (Case Study: Yalamlam Area, Saudi Arabia). *Water* **2022**, *14*, 897. [CrossRef]
21. Al-Amri, N.S.; Subyani, A.M. Generation of Rainfall Intensity Duration Frequency (IDF) Curves for Ungauged Sites in Arid Region. *Earth Syst. Environ.* **2017**, *1*, 8. [CrossRef]

22. Fadhel, S.; Al Aukidy, M.; Saleh, M.S. Uncertainty of intensity-duration-frequency curves due to adoption or otherwise of the temperature climate variable in rainfall disaggregation. *Water* **2021**, *13*, 2337. [CrossRef]
23. Sun, Y.; Wendi, D.; Kim, D.E.; Liong, S.Y. Deriving intensity–duration–frequency (IDF) curves using downscaled in situ rainfall assimilated with remote sensing data. *Geosci. Lett.* **2019**, *6*, 17. [CrossRef]
24. Hershenhorn, J.S.; Woolhiser, D.A. Disaggregation of Daily Rainfall. 1987. Available online: http://hdl.handle.net/10150/191279 (accessed on 12 August 2024).
25. Econopouly, T.W.; Davis, D.R.; Woolhiser, D.A. Parameter transferability for a daily rainfall disaggregation model. *J. Hydrol.* **1990**, *118*, 209–228.
26. Connolly, R.D.; Schirmer, J.; Dunn, P.K. A daily rainfall disaggregation model. *Agric. For. Meteorol.* **1998**, *92*, 105–117. [CrossRef]
27. Bo, Z.; Islam, S. Aggregation-disaggregation properties of a stochastic rainfall model. *Water Resour. Res.* **1994**, *30*, 3423–3436. [CrossRef]
28. Glasbey, A.C.A.; Cooper, G.; Mcgechan, M.B. Disaggregation of daily rainfall by conditional simulation from a point-process model. *J. Hydrol.* **1995**, *165*, 1–9. [CrossRef]
29. Koutsoyiannis, D.; Onof, C. Rainfall disaggregation using adjusting procedures on a Poisson cluster model. *J. Hydrol.* **2001**, *246*, 109–122. [CrossRef]
30. Burian, B.J.S.; Member, A.; Durrans, S.R.; Tomic, S.; Pimmel, R.L.; Wai, C.N. Rainfall disaggregation using artificial neural networks. *J. Hydrol. Eng.* **2000**, *5*, 299–307. [CrossRef]
31. Gaume, E.; Sivakumar, B.; Kolasinski, M.; Hazoumé, L. Identification of chaos in rainfall temporal disaggregation: Application of the correlation dimension method to 5-minute point rainfall series measured with a tipping bucket and an optical raingage. *J. Hydrol.* **2006**, *328*, 56–64. [CrossRef]
32. Sivakumar, B.; Sorooshian, S.; Gupta, H.V.; Gao, X. A chaotic approach to rainfall disaggregation. *Water Resour. Res.* **2001**, *37*, 61–72. [CrossRef]
33. Willems, P. *Impacts of Climate Change on Rainfall Extremes and Urban Drainage Systems*; IWA: Singapore, 2012.
34. Athar, H. Trends in observed extreme climate indices in Saudi Arabia during 1979–2008. *Int. J. Climatol.* **2014**, *34*, 1561–1574. [CrossRef]
35. Sultan, S.I. Wadi ar Rumah the Earth Longest Dry Watershed Analysis System Using Remote Sensing Thermal Data. 2011. Available online: https://iwra.org/proceedings/congress/resource/PAP00-5971.pdf (accessed on 12 November 2024).
36. Al-Gurairy, A.Y.; Mahmoud, A.S.; Aljibory, H.A. Source Rock of the Volcanic Fragments in Wadi Al-batin, Iraq: Geomorphological, Petrographical and Geochemical Evidences. *Int. J. Adv. Sci. Res. Manag.* **2017**, *2*, 37–50. Available online: www.ijasrm.com (accessed on 23 November 2024).
37. Authority for Statistics. Population Characteristics Surveys. Available online: https://portal.saudicensus.sa/portal/public/1/22/101479?type=TABLE (accessed on 14 October 2023).
38. MIT. Climate Models | Massachusetts Institute of Technology Climate Portal. Available online: https://climate.mit.edu/explainers/climate-models (accessed on 2 October 2023).
39. Maity, R. Statistical Methods in Hydrology and Hydroclimatology. 2018. Available online: http://www.springer.com/series/13593 (accessed on 13 August 2023).
40. Walpole, R.E.; Myers, R.H.; Myers, S.L.; Ye, K. *Probability & Statistics for Engineers & Scientists*, 9th ed.; Pearson: London, UK, 2012.
41. Ponce, V.M. *Engineering Hydrology, Principles and Practices*; Pearson College Div: London, UK, 1989.
42. Lee, T.; Singh, V.P. *Statistical Downscaling for Hydrological and Environmental Applications*; CRC Press: Boca Raton, FL, USA, 2019.
43. Cannon, A.J.; Sobie, S.R.; Murdock, T.Q. Bias correction of GCM precipitation by quantile mapping: How well do methods preserve changes in quantiles and extremes? *J. Clim.* **2015**, *28*, 6938–6959. [CrossRef]
44. Lall, U.; Sharma, A. A Nearest Neighbor Bootstrap For Resampling Hydrologic Time Series. *Water Resour. Res.* **1996**, *32*, 679–693. [CrossRef]
45. Subyani, A.M.; Al-Amri, N.S. IDF curves and daily rainfall generation for Al-Madinah city, western Saudi Arabia. *Arab. J. Geosci.* **2015**, *8*, 11107–11119. [CrossRef]
46. Ewea, H.A.; Elfeki, A.M.; Al-Amri, N.S. *Development of Intensity–Duration–Frequency Curves for the Kingdom of Saudi Arabia*; Taylor and Francis Ltd.: Abingdon, UK, 2017. [CrossRef]
47. Elsebaie, I.H. Developing rainfall intensity–duration–frequency relationship for two regions in Saudi Arabia. *J. King Saud Univ.-Eng. Sci.* **2012**, *24*, 131–140. [CrossRef]
48. Yan, H.; Sun, N.; Wigmosta, M.; Skaggs, R.; Hou, Z.; Leung, L.R. Next-Generation Intensity–Duration–Frequency Curves to Reduce Errors in Peak Flood Design. *J. Hydrol. Eng.* **2019**, *24*, 04019020. [CrossRef]
49. Ombadi, M.; Nguyen, P.; Sorooshian, S.; Hsu, K.L. Developing Intensity-Duration-Frequency (IDF) Curves From Satellite-Based Precipitation: Methodology and Evaluation. *Water Resour. Res.* **2018**, *54*, 7752–7766. [CrossRef]
50. Noor, M.; Ismail, T.; Shahid, S.; Asaduzzaman, M.; Dewan, A. Evaluating intensity-duration-frequency (IDF) curves of satellite-based precipitation datasets in Peninsular Malaysia. *Atmos. Res.* **2021**, *248*, 105203. [CrossRef]

51. Chitrakar, P.; Sana, A.; Almalki, S.H.N. Regional distribution of intensity–duration–frequency (IDF) relationships in Sultanate of Oman. *J. King Saud Univ. Sci.* **2023**, *35*, 102804. [CrossRef]
52. Zhu, J.; Stone, M.C.; Forsee, W. Analysis of potential impacts of climate change on intensity-duration-frequency (IDF) relationships for six regions in the United States. *J. Water Clim. Change* **2012**, *3*, 185–196. [CrossRef]
53. Noor, M.; Ismail, T.; Shahid, S.; Asaduzzaman, M.; Dewan, A. Projection of Rainfall Intensity-Duration-Frequency Curves at Ungauged Location under Climate Change Scenarios. *Sustain. Cities Soc.* **2022**, *83*, 103951. [CrossRef]
54. Molla, M. Statically Downscaling using different Representative Concentration Pass ways of Emission Scenario; in the Case Wolikite, South West Ethiopia. *Int. J. Environ. Sci. Nat. Resour.* **2020**, *25*, 556162. [CrossRef]
55. IPCC. *Intergovernmental Panel on Climate Change: IPCC (2007) Climate Change 2007, Synthesis Report (AR4)*; IPCC: Geneva, Switzerland, 2007.
56. ESCWA. *United Nations Economic and Social Commission for Western Asia*; ESCWA: Beirut, Lebanon, 2023; pp. 1–33.
57. Alodah, A. Assessment of Past Precipitation Extreme Events Over the Qassim Region in Saudi Arabia. In *Advances in Science, Technology and Innovation*; Springer Nature: Berlin/Heidelberg, Germany, 2023; pp. 253–256. [CrossRef]
58. Alzahrani, F.; Seidou, O.; Alodah, A. Assessment and Improvement of IDF Generation Algorithms Used in the IDF_CC Tool. *Water Resour. Manag.* **2022**, *36*, 4591–4606. [CrossRef]
59. Alzahrani, F.; Seidou, O.; Alodah, A. Assessing the Performance of Daily to Subdaily Temporal Disaggregation Methods for the IDF Curve Generation under Climate Change. *J. Water Clim. Change* **2023**, *14*, 1339–1357. [CrossRef]

Disclaimer/Publisher's Note: The statements, opinions and data contained in all publications are solely those of the individual author(s) and contributor(s) and not of MDPI and/or the editor(s). MDPI and/or the editor(s) disclaim responsibility for any injury to people or property resulting from any ideas, methods, instructions or products referred to in the content.